Comparative study of Ho:Y_2O_3 and Ho:Y_3Al5O_12 transparent ceramics produced from laser-ablated nanoparticles

Pavel Loiko, Liza Basyrova, Roman Maksimov, Vladislav Shitov, Mikhail Baranov, Florent Starecki, Xavier Mateos, Patrice Camy

▶ To cite this version:

Pavel Loiko, Liza Basyrova, Roman Maksimov, Vladislav Shitov, Mikhail Baranov, et al.. Comparative study of Ho:Y_2O_3 and Ho:Y_3Al5O_12 transparent ceramics produced from laser-ablated nanoparticles. Journal of Luminescence, 2021, 240, pp.118460. 10.1016/j.jlumin.2021.118460 . hal-03345597

HAL Id: hal-03345597
https://hal.science/hal-03345597

Submitted on 18 Nov 2022

Comparative study of Ho:Y_2O_3 and Ho:$Y_3Al_5O_{12}$ transparent ceramics produced from laser-ablated nanoparticles

Pavel Loiko[a,*], Liza Basyrova[a], Roman Maksimov[b,c], Vladislav Shitov[c], Mikhail Baranov[d], Florent Starecki[a], Xavier Mateos[e,f], and Patrice Camy[a]

[a]Centre de Recherche sur les Ions, les Matériaux et la Photonique (CIMAP), UMR 6252 CEA-CNRS-ENSICAEN, Université de Caen Normandie, 6 Boulevar du Maréchal Juin, 14050 Caen Cedex 4, France
[b]Ural Federal University, 19 Mira St., 620002 Ekaterinburg, Russia
[c]Institute of Electrophysics, Ural Branch of the Russian Academy of Sciences, 106 Amundsen St., 620016 Ekaterinburg, Russia
[d]ITMO University, 49 Kronverkskiy Pr., 197101 St. Petersburg, Russia
[e]Universitat Rovira i Virgili (URV), Física i Cristal·lografia de Materials i Nanomaterials (FiCMA-FiCNA), Marcel·li Domingo 1, 43007 Tarragona, Spain
[f]Serra Húnter Fellow
**Corresponding author, e-mail: pavel.loiko@ensicaen.fr*

Abstract: Ho:Y_2O_3 and Ho:$Y_3Al_5O_{12}$ transparent ceramics are fabricated by vacuum sintering at 1780 °C for 20 h from laser-ablated nanopowders (Ho:Y_2O_3 and Ho:Y_2O_3 + Al_2O_3) using ZrO_2 and TEOS as sintering aids, respectively. The sesquioxide ceramic exhibits smaller grain size (~5.4 μm), smaller content of pores (down to 6 ppm) and higher optical transmission (up to 82.2% at ~1 μm) than the garnet one. A detailed comparative spectroscopic study of the two ceramics is performed. For the $^5I_7 \rightarrow {}^5I_8$ Ho^{3+} transition, the maximum stimulated-emission cross-sections and the luminescence lifetimes are σ_{SE} = 0.57×10^{-20} cm^2 at 2087.1 nm and τ_{lum} = 10.92 ms (for the Ho:Y_2O_3 ceramic) and σ_{SE} = 1.70×10^{-20} cm^2 at 2090.8 nm and τ_{lum} = 7.04 ms (for the Ho:$Y_3Al_5O_{12}$ one) The rates of multiphonon relaxation are determined for both ceramics. For the Ho:Y_2O_3 ceramic, they do not exceed those for single-crystals. The crystal-field splitting of Ho^{3+} multiplets ($^5I_7$ and $^5I_8$) is determined at 12 K and analyzed using the barycenter plot. Due to its broadband emission properties, the Ho:Y_2O_3 ceramic is suitable for mode-locked lasers emitting above 2 μm.

Keywords: transparent ceramic; sesquioxide; garnet; microstructure; holmium ion; luminescence.

1. Introduction

Transparent ceramics are polycrystalline optical materials composed of closely packed single-crystalline grains of random orientation providing weak light scattering at the grain boundaries which is ensured by low density of pores and a lack of secondary phases. They can serve as laser host materials for doping with rare-earth ions (RE^{3+}) [1]. The research and technological development of transparent laser ceramics have progressed significantly since Ikesue *et al.* fabricated in 1995 a high quality Nd^{3+}-doped $Y_3Al_5O_{12}$ ceramic by a solid-state reaction method [2] leading to efficient laser action at ~1 µm [3]. It has been shown that ceramic laser materials provide several advantages as compared to the single-crystal counterparts, namely (i) lower fabrication temperatures which is of particular interest for high melting point materials [4], (ii) easier and more controllable doping by RE^{3+} ions reaching higher concentrations [5], (iii) the possibility to fabricate "mixed" [6] and composite [7] media, and (iv) mass production. The ceramics may maintain the desirable spectroscopic and thermal properties of the single crystals [8,9].

Typically, cubic materials are selected for the development of transparent laser ceramics, allowing to avoid additional scattering losses related to birefringence. Among the oxide materials, cubic garnets such as $RE_3Al_5O_{12}$ (RE = Lu, Y) [3,10] and sesquioxides A_2O_3 (A = Lu, Y, Sc or their mixture) [4,11,12] are mainly employed in the laser ceramic technology because of their good mechanical and thermo-optical properties.

During the past decades, transparent garnet and sesquioxide ceramics doped with Nd^{3+} and Yb^{3+} ions were studied for the development of lasers emitting at ~1 µm. Recently, the interest shifted towards coherent light sources emitting in the eye-safe spectral range of ~2 µm. They are attractive for a broad range of applications [13]: welding and engraving of plastics, remote sensing of the atmosphere and wind mapping, medical treatment, as well as frequency conversion into the mid-IR [14] and supercontinuum generation. Laser emission at ~2 µm is typically achieved using Tm^{3+} or Ho^{3+} ions. Among them, holmium ions (Ho^{3+}) provide laser emission slightly above 2 µm [15,16] thus avoiding the structured water vapor absorption in the atmosphere and better addressing the desired applications.

For Ho^{3+} doping, materials containing yttrium (Y^{3+}) ions as host-forming cations are desirable, e.g., yttrium aluminum garnet ($Y_3Al_5O_{12}$) or yttrium oxide (Y_2O_3). This is because of the exceptional closeness of the ionic radii of Y^{3+} and Ho^{3+} (0.900 Å and 0.901 Å for VI-fold oxygen coordination, respectively [17]) leading to a minimum structure distortion upon doping and expected weak concentration dependence of the thermal conductivity.

$Ho:Y_3Al_5O_{12}$ ceramics with laser quality have been previously fabricated by solid-state reactive sintering at 1760-1780 °C using α-Al_2O_3, Y_2O_3 and Ho_2O_3 powders (commercial or co-precipitated) and tetraethyl orthosilicate (TEOS) as a sintering aid [18-20]. Regarding $Ho:Y_2O_3$ ceramics, hot isostatic pressing (HIPing) at relatively low temperatures (down to 1450-1600 °C) was employed to avoid enhanced grain growth leading to entrapment of isolated pores within grains so that full densification and high optical quality can be achieved [21,22].

Commercial and/or co-precipitated powders have been mainly used for fabricating the $Ho:Y_3Al_5O_{12}$ and $Ho:Y_2O_3$ ceramics. Typically, the fabrication process of $Y_3Al_5O_{12}$ ceramics includes planetary ball milling stage to crush hard agglomerates and to achieve the required dispersity and homogeneous mixing of raw oxide powders. This may cause measurable contamination of the mixture by alumina from the milling media and milling jars. Thus, it may be difficult to maintain a strict proportion of (RE + Y) / Al = 3 / 5 which is rather important as even small deviations from the stoichiometry may lead to an incomplete solid-state reaction and formation of secondary phases acting as scattering centers. Regarding Y_2O_3 ceramics, the main drawback of the existing fabrication methods consists of the use of the expensive

HIPing technique. Moreover, encapsulation of the pre-sintered ceramic with platinum is needed to prevent penetration of the pressurizing medium (Ar gas) inside the sample.

Ultrafine particles exhibiting high sintering activity can be used to overcome the above-mentioned difficulties. For example, nanopowders produced by laser ablation are beneficial for the fabrication of sesquioxide laser ceramics [23-26] because in this case, it is possible to achieve homogeneous mixing of the required components (the activator, the host material and the sintering additive) at the atomic scale. This enables the fabrication of ceramic samples with laser quality by vacuum sintering. As for laser ceramics with a garnet structure, a soft mixing procedure can be used instead of the planetary ball milling as nanoparticles are weakly agglomerated. This approach allowed to precisely control the stoichiometry leading to good optical quality [27,28].

The aim of the present work was to fabricate two Ho^{3+}-doped ceramics containing yttrium host-forming cations ($Y_3Al_5O_{12}$ and Y_2O_3) using laser-ablated nanoparticles, and to perform a comparative study of their structure and spectroscopic properties, with the goal of developing ceramic gain materials for ~2 µm lasers. Recently, preliminary laser results with a similar $Ho:Y_3Al_5O_{12}$ ceramic were reported without describing the material properties [29].

2. Fabrication of ceramic samples

2.1. $Ho:Y_3Al_5O_{12}$ ceramic

The ceramic samples have been fabricated at the Institute of Electrophysics UrB RAS (Ekaterinburg, Russia) using nano-sized particles synthesized by laser ablation [30]. The solid targets for ablation were prepared from commercial Ho_2O_3 and Y_2O_3 oxide powders mixed in the proportion of $(Ho_{0.01}Y_{0.99})_2O_3$ and commercial Al_2O_3 powder. To prepare the $Ho:Y_3Al_5O_{12}$ ceramics, the nanopowders of $Ho:Y_2O_3$ and Al_2O_3 were weighed according to the stoichiometric formula $(Ho_{0.01}Y_{0.99})_3Al_5O_{12}$ and then mixed in a rotary mixer with an inclined rotation axis with an addition of 0.5 wt% of tetraethyl orthosilicate (TEOS) as a sintering aid. The slurry was dried using a vacuum rotary evaporator and subsequently annealed at 600 °C for 3 h to remove the organic components. To prepare a powder sample containing a certain amount of cubic garnet phase, the powder mixture was compacted into a pellet with a relative density of 20% and calcined at 1200 °C for 3 h in air. Since the laser-ablated nanoparticles are fine and have high reactivity, the formation of the garnet phase starts well before completing the active shrinkage that causes significant changes in density of the powder compact. Thus, the pre-calcining step was found to be important for achieving a partial phase transformation to the stable garnet structure beneficial for the subsequent homogeneous densification [29]. After pre-calcining, the pellet was ball-milled in ethyl alcohol with yttrium stabilized zirconia (YSZ) balls for 48 h, dried and annealed at 600 °C for 3 h. The obtained powder was uniaxially dry-pressed at a pressure of 200 MPa to achieve a 15 mm-diameter disk with a thickness of about 3 mm. After the organic components were removed by annealing at 800 °C, the powder compact was vacuum sintered at 1780 °C for 20 h in a furnace with graphite heaters at a pressure of 10^{-5} mbar. Subsequently, the sintered sample was annealed at 1300 °C for 5 h in air and mirror-quality polished on both surfaces.

2.2. $Ho:Y_2O_3$ ceramic

For the fabrication of the $Ho:Y_2O_3$ ceramics, the solid target for laser ablation was prepared from Ho_2O_3 and Y_2O_3 powders dry-mixed in the proportion $(Ho_{0.01}Y_{0.99})_2O_3$ with a small addition of zirconium dioxide (ZrO_2) as grain growth inhibitor. The synthesized $Ho:Y_2O_3$ nanopowder was annealed at 1100 °C for 3 h to transform the metastable monoclinic phase into the main cubic one (C-type). Then it was uniaxially dry-pressed at 300 MPa to achieve a 15 mm-diameter cylindrical pellet. After removing the organic components by calcining at 800 °C for 3 h, the green pellet was vacuum sintered at 1780 °C for 20 h at a pressure of 10^{-5} mbar. The ceramic sample was annealed at 1400 °C for 2 h to eliminate the oxygen vacancies and mirror-quality polished on both surfaces.

A photograph of the annealed and double-side polished ceramic disks is shown in Fig. 1. The ceramics were transparent and, depending on the illumination, presented slight yellow (or rose) coloration determined by the Ho^{3+} doping.

3. Experimental

The content of Ho^{3+} ions in the as-synthesized Ho:Y_2O_3 nanopowder was determined by inductively coupled plasma mass spectrometry (ICP-MS) using an Optima 2100 DV spectrometer (PerkinElmer).

The X-ray powder diffraction (XRD) patterns of the ceramic samples were measured with a Shimadzu XRD-6000 diffractometer, Cu Kα radiation and a Ni filter. The microstructure of the fractured surface of the ceramics was characterized by scanning electron microscopy (SEM) using a MERLIN SEM microscope (Carl Zeiss). The grain size distribution was obtained by direct counting method (for >100 grains) using the ImageJ software. The shape factor of 1.2 was applied. The distribution of scattering centers throughout the depth of the ceramic disks was analyzed using an Olympus BX51TRF optical microscope.

The RT Raman spectra were measured using a confocal Raman microscope (Renishaw inVia) with a ×50 objective (Leica) and an edge filter. The excitation source was an Ar^{+} ion laser (514 nm).

The transmission spectra of the ceramics in the visible and near-IR were measured using a spectrophotometer (Lambda 1050, Perkin Elmer and Shimadzu UV-PC 3101) while in the mid-IR – using a FTIR spectrometer Bruker Tensor 27. The luminescence spectra of the Ho^{3+} ions were measured using an optical spectrum analyzer (AQ6375B, Yokogawa) and a home-made Tm-laser (λ = 2010 nm) as excitation source. For low-temperature (LT, 12 K) studies, the sample was mounted on an APD DE-202 closed-cycle cryo-cooler equipped with an APD HC 2 Helium vacuum cryo-compressor and a Laceshore 330 temperature controller. The Ho^{3+} luminescence at LT was excited by a 532 nm laser (Verdi G series, Coherent).

The luminescence decay curves were measured using a ns optical parametric oscillator (OPO, Horizon, Continuum), a 1/4 m monochomator (Oriel 77200), a photomultiplier (PMT) tube, an InGaAs detector and an 8 GHz digital oscilloscope (DSA70804B, Tektronix).

4. Characterization of ceramics

4.1. Structural study

According to the ICP-MS analysis, the actual concentration of Ho^{3+} ions in the Ho:Y_2O_3 laser-ablated nanopowder was 0.94±0.09 at.% (with respect to Y^{3+} ions). It determined the doping level for both ceramics. The Ho^{3+} ions density was calculated to be $N_{Ho} = 2.51\times10^{20}$ cm^{-3} (Ho:Y_2O_3) and 1.30×10^{20} cm^{-3} (Ho:$Y_3Al_5O_{12}$) assuming a density ρ of 5.01 g/cm^3 and 4.56 g/cm^3, respectively.

The impurity (transition-metal and rare-earth elements) composition of Al_2O_3, Ho:Y_2O_3 and Ho,Zr:Y_2O_3 nanopowders obtained by laser ablation and further used for the fabrication of ceramics obtained by the ICP-MS method is presented in Table 1.

The phase purity and the structure of the ceramics were confirmed by powder XRD, Fig. 2. Both ceramics are of single-phase nature. The Ho:Y_2O_3 ceramic has a cubic (bixbyite or C-type) structure with space group $Ia\bar{3}$ - T^7_h, No. 206 and a lattice constant a = 10.605 Å (for undoped Y_2O_3, a = 10.602 Å). The relative intensities and positions of the diffraction peaks for the ceramic well correspond to those for Y_2O_3 (ICSD card #86-1326)

[31]. In the bixbyite structure, two types of sites for rare-earth ions exist having C_2 and C_{3i} symmetry with VI-fold oxygen coordination. In the unit-cell, there are a total of 32 cationic positions: 24 (3/4) correspond to the C_2 sites and 8 (1/4) - to the C_{3i} ones. As Ho^{3+} ions are replacing the Y^{3+} ions, they are expected to follow approximately this distribution.

The Ho:$Y_3Al_5O_{12}$ ceramic has also cubic structure (sp. gr. $Ia\bar{3}d$ – O^{10}_h, No. 230) and its lattice constant a = 12.010 Å (for undoped $Y_3Al_5O_{12}$, a = 12.010 Å). The measured XRD pattern matches well with the ICSD card # 79-1892 for $Y_3Al_5O_{12}$ [32]. There exists one rare-earth site with D_2 symmetry and VIII-fold oxygen coordination (the Ho^{3+} ions are replacing for the Y^{3+} ones). Note that for both ceramics, almost no variation of the lattice constant with the Ho^{3+} doping was observed due to the closeness of ionic radii of Ho^{3+} and Y^{3+} (e.g., 1.015 Å and 1.019 for VIII-fold oxygen coordination, respectively [17]). The stoichiometric compounds Ho_2O_3 and $Ho_3Al_5O_{12}$ exist [33,34].

The microstructure of the fractured surface of the ceramics was studied by SEM, Fig. 3. The ceramics exhibit a close-packed microstructure and a relatively narrow grain size distribution. For the Ho:Y_2O_3 ceramic, the mean grain size D_{grain} is 5.4 μm and the intragranular fracture mechanism is observed. For the Ho:$Y_3Al_5O_{12}$ one, larger grains are observed, D_{grain} = 35.6 μm, and the intergranular fracture mechanism dominates. The mean grain size of the Ho:Y_2O_3 ceramic is smaller than that of the Ho:$Y_3Al_5O_{12}$ one because different sintering additives corresponding to opposite densification mechanisms were employed: TEOS used for the fabrication of the Ho:$Y_3Al_5O_{12}$ ceramic promotes densification and grain growth due to formation of liquid phase while ZrO_2 suppresses the grain boundary mobility owing to formation of solid solution in the grain boundary regions of the Ho:Y_2O_3 ceramic.

The distribution of scattering centers in the ceramic samples throughout their depth is shown in Fig. 4. The average volume fraction of the scattering centers was 6 ppm and 25.7 ppm for the best Ho:Y_2O_3 and Ho:$Y_3Al_5O_{12}$ samples, respectively. The difference can be attributed to overheating of the Ho:$Y_3Al_5O_{12}$ ceramic that led to an enhanced grain growth and entrapment of larger amount of pores within the grains.

The vibronic properties of the ceramics were studied by Raman spectroscopy. The RT Raman spectrum of the Ho:Y_2O_3 ceramic is shown in Fig. 5. The structure of cubic Y_2O_3 is body-centered and the unit-cell contains the primitive cell twice (the number of the formula units per unit cell Z = 16). Thus, only 8 formula units are used to determine the number of vibrations. At the center of the Brillouin zone, the set of irreducible representations for optical modes is as follows: $\Gamma = 4A_g + 4E_g + 14F_g + 5A_{2u} + 5E_u + 16F_u$, among which all the even (*gerade*) modes A_g, E_g, and F_g are Raman active (22 in total), F_u is IR active and A_{2u} and E_u are silent [35,36]. The number of the observed modes is less than the theoretical one. The spectrum is dominated by an intense band at 376 cm^{-1} assigned to a combination of an A_g and a F_g mode and related to stretching vibrations. In the range of small frequencies, there are three well resolved lines characteristic of the C-type structure, centered at 192, 159 and 128 cm^{-1} and related to $E_g + F_g$, $A_g + F_g$ and F_g modes, respectively. The maximum phonon frequency is ~592 cm^{-1}.

For the Ho:$Y_3Al_5O_{12}$ ceramic, the Raman spectrum was strongly overlapping with the Ho^{3+} luminescence.

4.2. Optical transmission and absorption

Typical overview transmission spectra of the ceramics in the visible and IR are shown in Fig. 6. For the Ho:Y_2O_3 ceramic, the transparency range is broad, 0.24 – 9.4 μm, and for the Ho:$Y_3Al_5O_{12}$, it is narrower, 0.26 – 6.4 μm. The structured absorption bands are due to the intra 4f-shell electronic transitions of the dopant Ho^{3+} ions (electronic configuration: [Xe]$4f^{10}$).

For the best-transmitting samples, the in-line transmission at ~1 μm (out of the Ho^{3+} absorption range) was as follows: for the $Ho:Y_2O_3$ ceramic disk (thickness, t = 1.3 mm), it amounted to T = 82.2% being close to the theoretical limit set by Fresnel losses, $T_0 = 2n/(n^2 + 1)$, accounting for the multiple light reflections (T_0 = 82.7%, for n = 1.8903 [37]) and for the $Ho:Y_3Al_5O_{12}$ ceramic disk (t = 1.8 mm), the transmission was lower, T = 81.2%, compared with the theoretical one, T_0 = 84.5% assuming n = 1.816 [38], due to the presence of larger amount of residual pores as shown above.

The absorption spectra of Ho^{3+} ions in both ceramics were measured in detail and plotted in Fig. 7 in terms of the absorption coefficient, $\alpha_{abs} = -\ln(T/T_0)/t$. The assignment of the excited multiplets follows the one by Carnall *et al.* [39]. The absorption bands are due to transitions of Ho^{3+} ions from the ground-state, $^5I_8$, to the excited-states from $^5I_7$ (at ~2 μm) up to $^3M_{10} + {}^3L_3 + ({}^5G, {}^5D, {}^3G)_3 + ({}^3F, {}^3G)_3$ (at ~0.29 μm). The assignment of transitions deeper in the UV is complicated because they spectrally overlap with each other and simultaneously are superimposed on the UV absorption edge. The wave functions in the intermediate coupling scheme corresponding to states (energy levels) of rare-earth ions are linear combinations of wave functions in the Russell-Saunders approximation (the L-S coupling scheme). Typically, the energy levels are designated by indicating one or more L-S wave functions which contribute mainly to this linear combination. For designating high-lying excited-states of Ho^{3+} ions (see Fig. 7), we used this system.

Among the Ho^{3+} transitions, one should highlight the $^5I_8 \rightarrow {}^3K_8 + {}^5G_6 + {}^5F_1$ one around ~0.46 μm. Due to the proximity of these multiplets, it is difficult to separate the corresponding absorption bands. The intensity of this Ho^{3+} transition is significantly higher for the Y_2O_3 ceramic as compared to the $Y_3Al_5O_{12}$ one. It is known as a “hypersensitive” one, i.e., its intensity depends significantly on both the structural characteristics and the type of ligands [40]. The two conditions for observing a “hypersensitive” transition are (i) the selection rules $\Delta J \leq 2$, $\Delta L \leq 2$ and (ii) the relations between the corresponding reduced squared matrix elements, $U^{(2)} \neq 0$ and $U^{(2)} \gg U^{(4)}, U^{(6)}$. According to these criteria, the “hypersensitive” behavior originates from the $^3K_8 + {}^5G_6$ states. By inspecting the absorption spectra, another “hypersensitive” transition at ~0.36 μm is observed ($^5I_8 \rightarrow ({}^5G,{}^3H)_5 + {}^3H_6 + ({}^5F,{}^3F,{}^5G)_2$).

For the $^5I_8 \rightarrow {}^5I_7$ Ho^{3+} transition at ~2 μm which is of interest for laser applications (for in-band or resonant excitation of ions directly to the upper laser level), the absorption cross-section spectra were calculated, $\sigma_{abs} = \alpha_{abs}/N_{Ho}$. Note that for sesquioxides, for rare-earth ions located in C_{3i} sites, the electric dipole (ED) transitions are forbidden due to the presence of a center of inversion and only magnetic dipole (MD) transitions following the selection rules $\Delta J = 0, \pm 1$, except of $0 \leftrightarrow 0'$ are allowed. Thus, some authors evaluate the cross-sections by considering only the RE^{3+} ions in C_2 sites (about 3/4 of the total ion density). There are two arguments against this in our case. First, the $^5I_8 \rightarrow {}^5I_7$ Ho^{3+} transition is MD allowed and it can have a contribution from ions in C_{3i} sites. Second, the actual distribution of rare-earth dopants in sesquioxide ceramics may vary from the one for ideal single-crystals. Thus, for $Ho:Y_2O_3$, we consider σ_{abs} as an “effective” value.

For the $Ho:Y_3Al_5O_{12}$ ceramic, the maximum $\sigma_{abs} = 1.28\times10^{-20}$ cm^2 at 1907.2 nm and the corresponding absorption bandwidth (full width at half maximum, FWHM) is 4.7 nm. For the $Ho:Y_2O_3$ ceramic, it is lower, $\sigma_{abs} = 0.80\times10^{-20}$ cm^2 at 1935.6 nm, while the corresponding absorption bandwidth is much broader, FWHM = 16.6 nm, Fig. 8.

4.3. Emission (spectra and lifetime)

The near-IR emission spectra of the studied ceramics were measured under direct excitation by a Tm-laser. The ceramics exhibited intense and broadband luminescence spanning from 1.82 to 2.2 μm, related to the $^5I_7 \rightarrow {}^5I_8$ Ho^{3+} transition.

The corresponding stimulated-emission (SE) cross-sections, σ_{SE}, were derived by two methods. First is the Füchtbauer–Ladenburg (F-L) equation [41]:

$$\sigma_{\mathrm{SE}}(\lambda) = \frac{\lambda^5}{8\pi\langle n\rangle^2 \tau_{\mathrm{rad}} c} \frac{W'(\lambda)}{\int W'(\lambda)\mathrm{d}\lambda}, \tag{1}$$

where, λ is the light wavelength, $<n>$ is the refractive index corresponding to the average emission wavelength $<\lambda_{lum}>$, τ_{rad} is the radiative lifetime of the emitting state ($^5I_7$ state of Ho^{3+}), c is the speed of light and $W'(\lambda)$ is the luminescence spectrum calibrated for the apparatus function of the set-up. For transitions with reabsorption, the measured luminescence spectrum can be affected especially at shorter wavelengths.

The reciprocity method (RM, also called the McCumber relation) is the second method used [42]:

$$\sigma_{\mathrm{SE}}(\lambda) = \sigma_{\mathrm{abs}}(\lambda)\, \frac{Z_1}{Z_2} \mathrm{e}^{-\left(\frac{h\nu - E_{\mathrm{ZPL}}}{kT}\right)}, \tag{2}$$

where, h is the Planck constant, v is the light frequency, k is the Boltzmann constant, T is the temperature (RT), E_{ZPL} is the energy of the zero-phonon-line (ZPL) transition between the lowest Stark sub-levels of the two multiplets ($^5I_7$ and $^5I_8$ states of Ho^{3+}), $Z_{1(2)}$ are the partition functions of the lower and upper manifolds, respectively:

$$Z_m = \sum\nolimits_k g_k^m \mathrm{e}^{-\frac{E_k^m}{kT}}, \tag{3}$$

where each Stark sub-level has a number k, an energy $E^m{}_k$ measured from the lowest sub-level of each multiplet and a degeneracy $g^m{}_k$. For the calculations, we used the data on the crystal-field splitting of the $^5I_7$ and $^5I_8$ Ho^{3+} multiplets achieved in the present work (Section 4.4). Due to the exponential term in Eq. (2), a significant error from the RM calculations raises for light wavelengths well above the ZPL transition.

The results on σ_{SE} calculated by the two methods are shown in Fig. 8. The derivation of the radiative lifetime τ_{rad} is not a straightforward task. Theoretically, it can be calculated by means of the Judd-Ofelt theory based on the absorption spectra, e.g., the calculated $\tau_{rad}(^5I_7)$ is 13.19 ms for $Ho:Y_2O_3$ [43] and 7.82 ms for $Ho:Y_3Al_5O_{12}$ [44]. On the other hand, the simultaneous use of the F-L and RM approaches allows for the estimation of τ_{rad} from the comparison of the σ_{SE} spectra. In the present work, the following values are achieved: $\tau_{rad}(^5I_7) = 13.5 \pm 0.4$ ms for $Ho:Y_2O_3$ and 7.6 ± 0.2 ms for $Ho:Y_3Al_5O_{12}$ which reasonably agree with the results from the Judd-Ofelt analysis [43,44].

The $^5I_7 \rightarrow {}^5I_8$ Ho^{3+} transition represents a quasi-three-level scheme with reabsorption. Thus, the actual laser wavelength will be typically longer than the ZPL. In this spectral range, the maximum SE cross-sections σ_{SE} amount to 0.57×10^{-20} cm^2 at 2087.1 nm for the $Ho:Y_2O_3$ ceramic (F-L method) and 1.70×10^{-20} cm^2 at 2090.8 nm for the $Ho:Y_3Al_5O_{12}$ one (RM). The lower σ_{SE} value for the former material is due to two reasons: (i) broader emission spectra and (ii) much longer radiative lifetime of the emitting state.

The Ho^{3+} ions are also known for their visible emission falling in the green spectral range. The corresponding luminescence spectra are shown in Fig. 9. The emission spans from 0.53 to 0.56 µm being related to transitions from the closely located (thermally coupled) $^5F_4$ and $^5S_2$ excited-states to the $^5I_8$ ground-state. The emission maxima are at 551.3 nm for $Ho:Y_2O_3$ and 541.5 nm for $Ho:Y_3Al_5O_{12}$.

The luminescence decay curves from the $^5I_7$, $^5I_6$, $^5F_5$ and $^5F_4 + {}^5S_2$ excited states were measured at RT under pulsed excitation, Fig. 10. The luminescence decay from the $^5I_5$ and $^5I_4$ multiplets was faster than ~0.5 µs. To avoid the possible effect of reabsorption (radiation trapping) on the measured decay curves, the ceramic samples were finely powdered and a very thin powder layer (<50 µm) on a transparent substrate was formed.

For laser applications of the ceramics, the Ho^{3+} multiplet of main interest is the $^5I_7$. The decay curves plotted in a semi-log scale reveal a single-exponential decay for both ceramics, Fig. 10(a). The luminescence lifetime τ_{lum} was determined using the formula $I_{PL}(t) = I_0\times\exp(-t/\tau_{lum})$, where t is time. It amounted to 10.92 ms for the $Ho:Y_2O_3$ ceramic and 7.04 ms for the $Ho:Y_3Al_5O_{12}$ one.

The measured luminescence lifetime of the $^5I_7$ Ho^{3+} multiplet can be shortened with respect to the radiative one τ_{rad} owing to the multiphonon non-radiative (NR) relaxation:

$$\frac{1}{\tau_{\mathrm{lum}}} = \frac{1}{\tau_{\mathrm{rad}}} + W_{\mathrm{NR}}, \tag{4}$$

where W_{NR} is the multiphonon rate expressed in [s^{-1}]. Using Eq. (4), we estimate the values of W_{NR} for the $^5I_7 \rightarrow {}^5I_8$ Ho^{3+} transition as 15.7 s^{-1} for the $Ho:Y_2O_3$ ceramic and 14.2 s^{-1} for the $Ho:Y_3Al_5O_{12}$ one.

The luminescence quantum yield from the $^5I_7$ Ho^{3+} state can be estimated as:

$$\eta_{\mathrm{q}} = \frac{\tau_{\mathrm{lum}}}{\tau_{\mathrm{rad}}}. \tag{5}$$

This equation gives η_q = 82.8% and 90.0% for the $Ho:Y_2O_3$ and $Ho:Y_3Al_5O_{12}$ ceramics, respectively (the τ_{rad} values from [43,44] obtained by the Judd-Ofelt theory were used). Lower η_q value for the former ceramic is partially referred to the higher Ho^{3+} ion density in sesquioxides as compared to garnets (under the same doping level in at.%).

Note that for higher-lying excited-states of Ho^{3+} ions in the $Ho:Y_3Al_5O_{12}$ ceramic, the luminescence lifetimes are significantly shorter than for the $Ho:Y_2O_3$ one, e.g., for the green-emitting levels $^5S_2$ + $^5F_4$, τ_{lum} is 3.47 μs and 103.7 μs, respectively. To understand better this difference, the rates of the multiphonon relaxation for the $^5I_7$, $^5I_6$ and $^5S_2$ + $^5F_4$ states were plotted as a function of the energy-gap to the lower-lying multiplet ΔE using a semi-log scale, as shown in Fig. 11. The $^5F_5$ state was excluded from the analysis due to its too short, measured lifetime which can be affected by the response of the detector. The evaluation of W_{NR} values is presented in Table 2.

The dependence of W_{NR} on ΔE at a fixed temperature (RT) is expressed by the following equation [45]:

$$W_{\mathrm{NR}}(JJ') = C\mathrm{e}^{-\alpha\Delta E(JJ')}, \tag{6}$$

where C and α are the constants which are determined by the host matrix: C has the meaning of the multiphonon rate at the limit of zero energy gap and α:

$$\alpha = -\ln(\varepsilon)/h\nu_{\mathrm{ph}}, \tag{7}$$

where ε is the ratio between the probabilities of m-phonon and (m–1)-phonon relaxation, and $h\nu_{ph}$ is the maximum phonon energy of the host matrix mainly contributing to the NR relaxation. Thus, for materials with smaller phonon energies, weaker multiphonon rates are expected. This agrees well with our observations for Y_2O_3 and $Y_3Al_5O_{12}$ ceramics having different vibronic properties (the maximum phonon energy $h\nu_{ph,max}$ for the latter material is ~780 cm^{-1}).

The fit of the experimental points in Fig. 11 using Eq. (6) yields the following parameters: $C = 2.95\pm0.1\times10^7$ s^{-1} and $\alpha = 3.1\pm0.15\times10^{-3}$ cm for the $Ho:Y_2O_3$ ceramic and $C = 4.0\pm0.2\times10^{11}$ s^{-1} and $\alpha = 5.1\pm0.3\times10^{-3}$ cm for the $Ho:Y_3Al_5O_{12}$ one. The ratio of α parameters for these two materials ($Y_3Al_5O_{12}$ / Y_2O_3) is ~1.6 which allows us to identify the Raman modes contributing to multi-phonon processes in $Ho:Y_2O_3$ ceramic, ~470-480 cm^{-1}, which are easily found in the measured Raman spectrum, cf. Fig. 5.

It is known that the multiphonon processes are weak if the energy-gap to the lower-lying multiplet well exceeds the phonon energy of the host [46]:

$$\frac{\Delta E}{h\nu_{\mathrm{ph}}} \geq 4-5, \tag{8}$$

which is the so-called “energy gap” law. It is thus not surprising that for the $^5I_7$ Ho^{3+} multiplet in both ceramics, the multiphonon rates are weak and even comparable despite the difference in the phonon energies of the host matrices. The corresponding ΔE = 4698 cm^{-1} (Ho:Y_2O_3) and 4685 cm^{-1} (Ho:$Y_3Al_5O_{12}$), so that the condition in Eq. (8) is well satisfied.

In general, the parameters of the multiphonon relaxation should weakly depend on the rare-earth ion. In the literature, there is no information about W_{NR} for Y_2O_3 single crystals doped with Ho^{3+} while there exist studies for other ions, e.g., Er^{3+} [47]. The data for crystalline Er:Y_2O_3 are also shown in Fig. 11. The conclusion is that the developed ceramic shows a very similar multiphonon relaxation as compared to the corresponding single-crystal.

4.4. Low-temperature spectroscopy

LT (12 K) absorption and emission spectroscopy was used to determine the crystal-field splitting of the $^5I_8$ and $^5I_7$ Ho^{3+} multiplets which are relevant for laser applications, Fig. 12. The LT absorption spectra were plotted vs. the light wavenumber revealing the excited-state splitting. The LT emission spectra were plotted vs. (E_{ZPL} – wavenumber) revealing the splitting of the ground-state.

For both the C_2 and D_2 sites, each $^{2S+1}L_J$ multiplet with an integer J is split into $2J + 1$ sub-levels (17 for $^5I_8$ and 15 for $^5I_7$). Following the previous studies, all of them were identified (knowing that for the $^5I_7$ multiplet, several Stark sub-levels practically coincide) [44,48]. The resulting crystal-field splitting for the $^5I_8$ and $^5I_7$ Ho^{3+} multiplets in Y_2O_3 ceramic (C_2 sites) and $Y_3Al_5O_{12}$ ceramic (D_2 sites) is shown in Fig. 13. The partition functions were then calculated using Eq. (3), namely Z_1 = 7.342, Z_2 = 8.269 and Z_1/Z_2 = 0.888 for the Ho:Y_2O_3 ceramic and Z_1 = 7.260, Z_2 = 9.460 and Z_1/Z_2 = 0.767 for the Ho:$Y_3Al_5O_{12}$ one. The ZPL energies for these two ceramics E_{ZPL} are 5158 cm^{-1} (the corresponding wavelength is 1938.7 nm) and 5229 cm^{-1} (1912.4 nm), respectively.

Gruber *et al.* calculated the crystal-field splitting for the ground-state ($^5I_8$) of Ho^{3+} ions in C_{3i} sites in crystalline Y_2O_3 [49]. However, we are unable to unambiguously identify the peaks assigned to C_{3i} sites in the measured LT emission spectrum, which can be due to the line broadening in ceramics or simply because of the predominant excitation of the ions in C_2 sites. In the LT absorption spectrum of this ceramic, several extra peaks are found (at 5146, 5169, 5209, 5222 cm^{-1}, etc.) which are probably due to the C_{3i} sites.

For trivalent rare-earth ions, the barycenter energy of any $^{2S+1}L_J$ multiplet belonging to the $4f^n$ shell should show a linear variation with the barycenter energy of any other isolated $^{2S'+1}L'_{J'}$ $4f^n$ multiplet. This dependence is represented by the so-called barycenter plot [50]; the concept developed by Antic-Fidancev. It is well known for Yb^{3+} [50] and recently, it was also proposed for Tm^{3+} [51]. In the present work, we present such an analysis for the $^5I_8$ and $^5I_7$ multiplets of Ho^{3+} ions. In Fig. 14, the barycenter energy of the first excited-state, $<E>(^5I_7)$, is plotted vs. that of the ground-state, $<E>(^5I_8)$. Neglecting the J-mixing, the energy separation between the two barycenters should be constant and equal to that for the free Ho^{3+} ion (~5030 cm^{-1}) [39]. Together with Y_2O_3 and $Y_3Al_5O_{12}$ studied in the present work, the data on multiple Ho^{3+}-doped crystals were added to the graph; the corresponding Stark splittings can be found elsewhere. The linear fit of the data in Fig. 14 yields a formula $<E>(^5I_7) = 5052 + 0.95\times<E>(^5I_8)$ [cm^{-1}] in good agreement with the above considerations. The barycenter energies for Ho^{3+} ions in Y_2O_3 and $Y_3Al_5O_{12}$ ceramics agree well with the general trend confirming the correctness of the assignment of the Stark sub-levels.

5. Conclusions

To conclude, yttrium-based sesquioxide and garnet ceramics (Y_2O_3 and $Y_3Al_5O_{12}$) obtained by vacuum sintering from laser-ablated nanopowders are suitable host materials for doping with holmium ions. In terms of the microstructure and optical properties, the Ho:Y_2O_3 ceramic offers smaller mean grain size (5.4 μm) and smaller content of μm-sized pores (about 6 ppm), as well as higher transmission at ~1 μm (T = 82.2%) close to the theoretical one and broader transparency range (0.24 – 9.4 μm), as compared to the garnet one.

Regarding the absorption and emission at ~2 μm (the $^5I_8 \leftrightarrow {}^5I_7$ Ho^{3+} transition which is of interest for laser applications), the garnet ceramics ensures higher transition cross-sections at the expense of narrower bandwidths. The radiative lifetimes of the $^5I_7$ Ho^{3+} state are 13.5±0.4 ms and 7.6±0.2 ms for the Ho:Y_2O_3 and Ho:$Y_3Al_5O_{12}$ ceramics, respectively. The multiphonon relaxation rates are determined based on the lifetime measurements. We show that multiphonon relaxation in the Ho:Y_2O_3 ceramic is at least not faster than that in the corresponding single-crystals highlighting the good optical quality of the former material. The analysis based on the barycenter law is successfully applied to the $^5I_8$ and $^5I_7$ Ho^{3+} multiplets in various crystalline materials confirming the correctness of the determined crystal-field splitting in the studied ceramics.

The developed ceramics are promising for in-band pumped Ho lasers emitting above 2 μm (including thin-disk ones).

Acknowledgements

The reported study was funded by RFBR (Russia) according to the research project No. 21-53-15014 and CNRS (France) according to the project IEA No. 00432.

References

1. A. Ikesue, Y. L. Aung, Ceramic laser materials, Nature Photon. 2 (2008) 721-727.
2. A. Ikesue, I. Furusato, K. Kamata, Fabrication of polycrystalline, transparent YAG ceramics by a solid-state reaction method, J. Am. Ceram. Soc. 78 (1995) 225-228.
3. A. Ikesue, T. Kinoshita, K. Kamata, K. Yoshida, Fabrication and optical properties of high-performance polycrystalline Nd:YAG ceramics for solid-state lasers, J. Am. Ceram. Soc. 78 (1995) 1033-1040.
4. J. Lu, K. Takaichi, T. Uematsu, A. Shirakawa, M. Musha, K.I. Ueda, H. Yagi, T. Yanagitani, A.A. Kaminskii, Yb^{3+}:Y_2O_3 ceramics–a novel solid-state laser material, Jpn. J. Appl. Phys. 41 (2002) L1373-L1375.
5. V. Lupei, A. Lupei, S. Georgescu, T. Taira, Y. Sato, A. Ikesue, The effect of Nd concentration on the spectroscopic and emission decay properties of highly doped Nd:YAG ceramics, Phys. Rev. B 64 (2001) 092102-1-4.
6. W. Jing, P. Loiko, J. M. Serres, Y. Wang, E. Vilejshikova, M. Aguiló, F. Díaz, U. Griebner, H. Huang, V. Petrov, X. Mateos, Synthesis, spectroscopy, and efficient laser operation of “mixed” sesquioxide Tm:$(Lu,Sc)_2O_3$ transparent ceramics, Opt. Mater. Express 7 (2017) 4192-4202.
7. W. Liu, Y. Zeng, J. Li, Y. Shen, Y. Bo, N. Zong, P. Wang, Y. Xu, J. Xu, D. Cui, Q. Peng, Sintering and laser behavior of composite YAG/Nd:YAG/YAG transparent ceramics, J. Alloys Compd. 527 (2012) 66-70.
8. J. Li, Y. Wu, Y. Pan, W. Liu, J. Huang, J. Guo, Fabrication, microstructure and properties of highly transparent Nd:YAG laser ceramics, Opt. Mater. 31 (2008) 6-17.
9. A. Ikesue, Y. L. Aung, T. Yoda, S. Nakayama, T. Kamimura, Fabrication and laser performance of polycrystal and single crystal Nd:YAG by advanced ceramic processing, Opt. Mater. 29 (2007) 1289-1294.
10. Y. Fu, J. Li, C. Wang, T. Xie, W. Li, L. Wu, Y. Pan, Fabrication and properties of highly transparent Yb:LuAG ceramics, J. Alloy Compd. 664 (2016) 595-601.
11. K. Takaichi, H. Yagi, A. Shirakawa, K. Ueda, S. Hosokawa, T. Yanagitani, A. A. Kaminskii, Lu_2O_3:Yb^{3+} ceramics–a novel gain material for high-power solid-state lasers, Phys. Status Solidi A. 202 (2005) R1-R3.
12. J. Lu, J. F. Bisson, K. Takaichi, T. Uematsu, A. Shirakawa, M. Musha, K. Ueda, H. Yagi, T. Yanagitani, A. A. Kaminskii, Yb^{3+}:Sc_2O_3 ceramic laser, Appl. Phys. Lett. 83 (2003) 1101-1103.

13. K. Scholle, S. Lamrini, P. Koopmann, P. Fuhrberg, 2 µm laser sources and their possible applications, in Frontiers in Guided Wave Optics and Optoelectronics, B. Pal, ed. (Intech, 2010), pp. 471–500.
14. P. A. Budni, L. A. Pomeranz, M. L. Lemons, C. A. Miller, J. R. Mosto, E. P. Chicklis, Efficient mid-infrared laser using 1.9-µm-pumped Ho:YAG and $ZnGeP_2$ optical parametric oscillators, J. Opt. Soc. Am. B 17 (2000) 723–728.
15. F. Wang, J. Tang, E. Li, C. Shen, J. Wang, D. Tang, D. Shen, Ho^{3+}:Y_2O_3 ceramic laser generated over 113 W of output power at 2117 nm, Opt. Lett. 44 (2019) 5933-5936.
16. H. Chen, D. Shen, J. Zhang, H. Yang, D. Tang, T. Zhao, X. Yang, In-band pumped highly efficient Ho:YAG ceramic laser with 21 W output power at 2097 nm, Opt. Lett. 36 (2011) 1575-1577.
17. R. D. Shannon, Revised effective ionic radii and systematic studies of interatomic distances in halides and chalcogenides, Acta Cryst. A. 32 (1976) 751-767.
18. W. X. Zhang, J. Zhou, W. B. Liu, J. Li, L. Wang, B. X. Jiang, Y. B. Pan, X. J. Cheng, J. Q. Xu, Fabrication, properties and laser performance of Ho:YAG transparent ceramic, J. Alloys Compd. 506 (2010) 745–748.
19. H. Yang, J. Zhang, X. Qin, D. Luo, J. Ma, D. Tang, H. Chen, D. Shen, Q. Zhang, Polycrystalline Ho:YAG transparent ceramics for eye-safe solid state laser applications, J. Amer. Ceram. Soc. 95 (2012) 52–55.
20. R. Lan, P. Loiko, X. Mateos, Y. Wang, J. Li, Y. Pan, S. Y. Choi, M. H. Kim, F. Rotermund, A. Yasukevich, K. Yumashev, U. Griebner, V. Petrov, Passive Q-switching of microchip lasers based on Ho:YAG ceramics, Appl. Opt. 55 (2016) 4877-4887.
21. G. A. Newburgh, A. Word-Daniels, A. Michael, L. D. Merkle, A. Ikesue, M. Dubinskii, Resonantly diode-pumped Ho^{3+}:Y_2O_3 ceramic 2.1 µm laser, Opt. Express 19 (2011) 3604-3611.
22. J. Wang, Y. Zhao, D. Yin, P. Liu, J. Ma, Y. Wang, D. Shen, Z. Dong, L. B. Kong, D. Tang, Holmium doped yttria transparent ceramics for 2-µm solid state lasers, J. Eur. Ceram. Soc. 38 (2018) 1986-1989.
23. S. N. Bagayev, V. V. Osipov, M. G. Ivanov, V. I. Solomonov, V. V. Platonov, A. N. Orlov, A. V. Rasuleva, S. M. Vatnik, Fabrication and characteristics of neodymium-activated yttrium oxide optical ceramics, Opt. Mater. 31 (2009) 740-743.
24. S. N. Bagayev, V. V. Osipov, V. A. Shitov, E. V. Pestryakov, V. S. Kijko, R. N. Maksimov, K. E. Lukyashin, A. N. Orlov, K. V. Polyakov, V. V. Petrov, Fabrication and optical properties of Y_2O_3-based ceramics with broad emission bandwidth, J. Eur. Ceram. Soc. 32 (2012) 4257-4262.
25. G. Toci, A. Pirri, B. Patrizi, R. N. Maksimov, V. V. Osipov, V. A. Shitov, A. S. Yurovskikh, M. Vannini, High efficiency emission of a laser based on Yb-doped $(Lu,Y)_2O_3$ ceramic, Opt. Mater. 83 (2018) 182-186.
26. G. Toci, A. Pirri, B. Patrizi, R. N. Maksimov, V. V. Osipov, V. A. Shitov, M. Vannini, Yb^{3+}:$(Lu_xY_{1-x})_2O_3$ mixed sesquioxide ceramics for laser applications. Part II: Laser performances, J. Alloys Compd. 853 (2021) 156943-1-8.
27. V. V. Osipov, R. N. Maksimov, V. A. Shitov, K. E. Lukyashin, G. Toci, M. Vannini, M. Ciofini, A. Lapucci, Fabrication, optical properties and laser outputs of Nd:YAG ceramics based on laser ablated and pre-calcined powders, Opt. Mater. 71 (2017) 45-49.
28. L. Basyrova, P. Loiko, R. Maksimov, V. Shitov, J. M. Serres, U. Greibner, V. Petrov, M. Aguilo, F. Diaz, X. Mateos, Comparative study of Yb:$Lu_3Al_5O_{12}$ and Yb:Lu_2O_3 laser ceramics produced from laser-ablated nanopowders, Ceram. Int. 47 (2021) 6633-6642.
29. S. N. Bagayev, V. V. Osipov, S. M. Vatnik, V. A. Shitov, I. A. Vedin, V. V. Platonov, I. Sh. Steinberg, R. N. Maksimov, Ho:YAG transparent ceramics based on nanopowders produced by laser ablation method: Fabrication, optical properties, and laser performance, Opt. Mater. 50 (2015) 47-51.
30. V. V. Osipov, V. V. Platonov, V. V. Lisenkov, A. V. Podkin, E. E. Zakharova, Production of nanopowders of oxides by means of fiber and pulse-periodical CO_2 lasers, Phys. Status Solidi C, 10 (2013) 926-932.
31. E. N. Maslen, V. A. Streltsov, N. Ishizawa, A synchrotron X-ray study of the electron density in C-type rare earth oxides, Acta Cryst. B 52 (1996) 414-422.

32. T. S. Chernaya, L. A. Muradyan, V. A. Sarin, E. M. Uyukin, K. S. Bagdasarov, V. I. Simonov, Neutron-diffraction structural investigation of single crystals of $Y_3Al_5O_{12}$:Nd^{3+}, Kristallografiya 34 (1989) 1292-1294.
33. D. Hu, X. Li, I. Snetkov, A. Yakovlev, S. Balabanov, M. Ivanov, X. Liu, Z. Liu, F. Tian, T. Xie, O. Palashov, Fabrication, microstructure and optical characterizations of holmium oxide (Ho_2O_3) transparent ceramics, J. Eur. Ceram. Soc. 41 (2021) 759-767.
34. A. O. Ivanov, I. V. Mochalov, A. M. Tkachuk, V. A. Fedorov, P. P. Feofilov, Emission of $\lambda \approx 2$ μ stimulated radiation by holmium in aluminum holmium garnet crystals, Sov. J. Quantum Electron. 5 (1975) 115-116.
35. N. D. Todorov, M. V. Abrashev, V. Marinova, M. Kadiyski, L. Dimowa, E. Faulques, Raman spectroscopy and lattice dynamical calculations of Sc_2O_3 single crystals, Phys. Rev. B 87 (2013) 104301.
36. A. Ubaldini, M. M. Carnasciali, Raman characterisation of powder of cubic RE_2O_3 (RE = Nd, Gd, Dy, Tm, and Lu), Sc_2O_3 and Y_2O_3, J. Alloys Compd. 454 (2008) 374-378.
37. A. A. Kaminskii, K. Ueda, A. F. Konstantinova, H. Yagi, T. Yanagitani, A. V. Butashin, V. P. Orekhova, J. Lu, K. Takaichi, T. Uematsu, M. Musha, A. Shirokava, Lasing and refractive indices of nanocrystalline ceramics of cubic yttrium oxide Y_2O_3 doped with Nd^{3+} and Yb^{3+} ions, Crystallogr. Rep. 48 (2003) 1041–1043.
38. D. E. Zelmon, D. L. Small, R. Page, Refractive-index measurements of undoped yttrium aluminum garnet from 0.4 to 5.0 μm, Appl. Opt. 37 (1998) 4933-4935.
39. W. T. Carnall, P. R. Fields, K. Rajnak, Electronic energy levels in the trivalent lanthanide aquo ions. I. Pr^{3+}, Nd^{3+}, Pm^{3+}, Sm^{3+}, Dy^{3+}, Ho^{3+}, Er^{3+}, and Tm^{3+}, J. Chem. Phys. 49 (1968) 4424-4442.
40. P. A. Ryabochkina, S. A. Antoshkina, E. V. Bolshakova, M. A. Ivanov, V. V. Kochurihin, A. V. Malov, S. N. Ushakov, N. V. Shchuchkina, K. N. Nishchev, Hypersensitive transitions of Tm^{3+}, Ho^{3+} and Dy^{3+} rare-earth ions in garnet crystals, J. Lumin. 132 (2012) 1900-1905.
41. B. Aull, H. Jenssen, Vibronic interactions in Nd:YAG resulting in nonreciprocity of absorption and stimulated emission cross sections, IEEE J. Quantum Electron. 18 (1982) 925-930.
42. S. A. Payne, L. L. Chase, L. K. Smith, W. L. Kway, W. F. Krupke, Infrared cross-section measurements for crystals doped with Er^{3+}, Tm^{3+} and Ho^{3+}, IEEE J. Quantum Electron. 28 (1992) 2619-2630.
43. K. L. Nash, R. C. Dennis, N. J. Ray, J. B. Gruber, D. K. Sardar, Absorption intensities, emission cross sections, and crystal field analysis of selected intermanifold transitions of Ho^{3+} in Ho^{3+}:Y_2O_3 nanocrystals, J. Appl. Phys. 106 (2009) 063117-1-8.
44. B. M. Walsh, G. W. Grew, N. P. Barnes, Energy levels and intensity parameters of Ho^{3+} ions in $Y_3Al_5O_{12}$ and $Lu_3Al_5O_{12}$, J. Phys. Chem. Sol. 67 (2006) 1567-1582.
45. M. J. Weber, Probabilities for radiative and nonradiative decay of Er^{3+} in LaF_3, Phys. Rev. 157 (1967) 262-272.
46. H. Scheife, G. Huber, E. Heumann, S. Bär, E. Osiac, Advances in up-conversion lasers based on Er^{3+} and Pr^{3+}, Opt. Mater. 26 (2004) 365-374.
47. M. J. Weber, Radiative and multiphonon relaxation of rare-earth ions in Y_2O_3, Phys. Rev. 171 (1968) 283-291.
48. R. P. Leavitt, J. B. Gruber, N. C. Chang, C. A. Morrison, Optical spectra, energy levels, and crystal-field analysis of tripositive rare-earth ions in Y_2O_3. II. Non-Kramers ions in C_2 sites, J. Chem. Phys. 76 (1982) 4775-4788.
49. J. B. Gruber, R. P. Leavitt, C. A. Morrison, N. C. Chang, Optical spectra, energy levels, and crystal-field analysis of tripositive rare-earth ions in Y_2O_3. IV. C_{3i} sites, J. Chem. Phys. 82 (1985) 5373-5378.
50. P. H. Haumesser, R. Gaumé, B. Viana, E. Antic-Fidancev, D. Vivien, Spectroscopic and crystal-field analysis of new Yb-doped laser materials," J. Phys. Cond. Matter 13 (2001) 5427-5447.
51. P. Loiko, L. Zhang, J. M. Serres, Y. Wang, M. Aguiló, F. Díaz, Z. Lin, H. Lin, G. Zhang, E. Vilejshikova, E. Dunina, A. Kornienko, L. Fomicheva, V. Petrov, U. Griebner, W. Chen, X. Mateos, Monoclinic Tm:$MgWO_4$ crystal: Crystal-field analysis, tunable and vibronic laser demonstration, J. Alloys Compd. 763 (2018) 581-591.

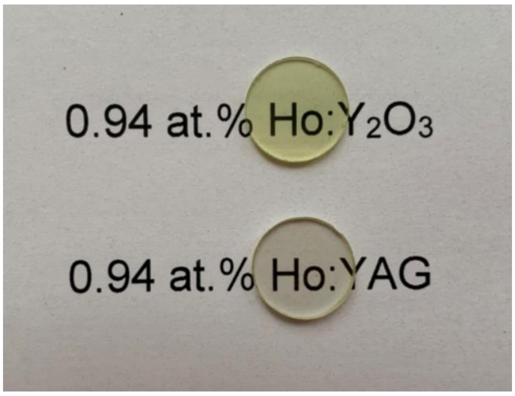

Fig. 1. Photograph of annealed and polished $Ho:Y_2O_3$ and $Ho:Y_3Al_5O_{12}$ transparent ceramic disks.

Table 1. Impurity composition of laser-ablated Al_2O_3, $Ho:Y_2O_3$ and $Ho,Zr:Y_2O_3$ nanopowders used for the fabrication of ceramics.

Content, ppm	Powder		
	Al_2O_3	$Ho:Y_2O_3$	$Ho,Zr:Y_2O_3$
Na	160	42	26
Mg	<1	1.9	<1
Ti	3	3	<1
V	<1	<1	<1
Cr	<1	4.9	1.7
Mn	<1	<1	<1
Fe	270	<1	<1
Co	<1	<1	<1
Ni	<1	<1	<1
Cu	4.2	1.9	<1
Zn	<1	26	4
La	1.3	<1	<1
Ce	<1	<1	<1
Pr	<1	<1	<1
Nd	3	2	<1
Sm	<1	<1	<1
Eu	<1	<1	<1
Gd	<1	<1	<1
Tb	<1	<1	<1
Dy	<1	<1	<1
Er	<1	1	<1
Tm	<1	<1	<1
Yb	<1	3.4	<1
Lu	<1	<1	<1
Hf	<1	<1	310

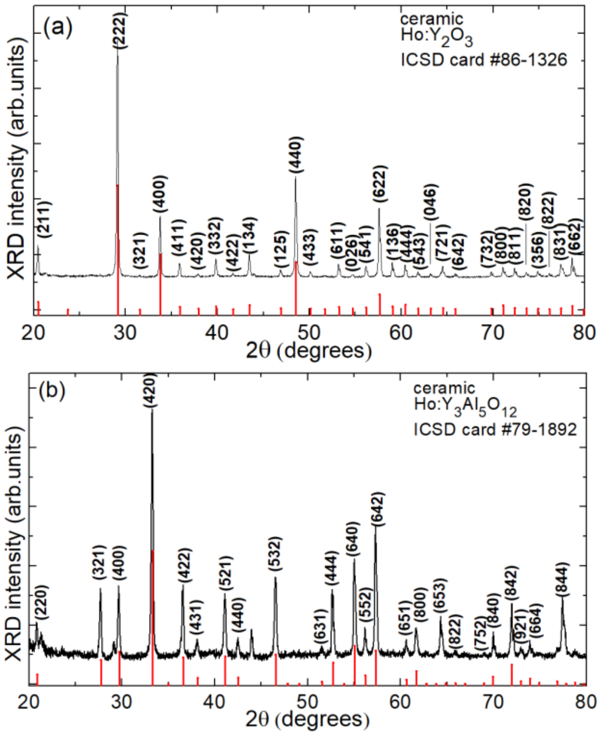

Fig. 2. X-ray powder diffraction (XRD) patterns of (a) Ho:Y_2O_3 and (b) Ho:$Y_3Al_5O_{12}$ ceramics, *vertical bars* – theoretical reflections for (a) Y_2O_3 (ICSD card # 86-1326) and (b) $Y_3Al_5O_{12}$ (ICSD card # 79-1892), (*hkl*) are the Miller's indices.

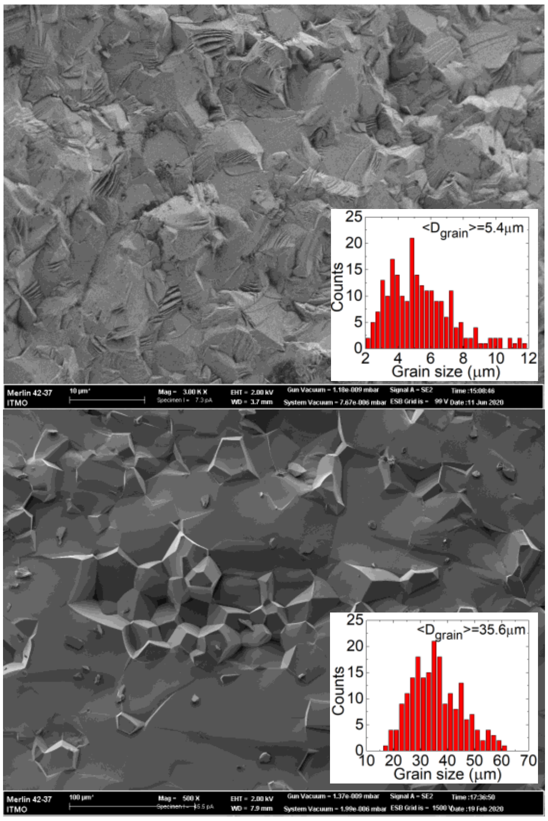

Fig. 3. Scanning Electron Microscope (SEM) images of the fractured surface of (a) Ho:Y_2O_3 and (b) Ho:$Y_3Al_5O_{12}$ ceramics, *insets* – grain size distributions.

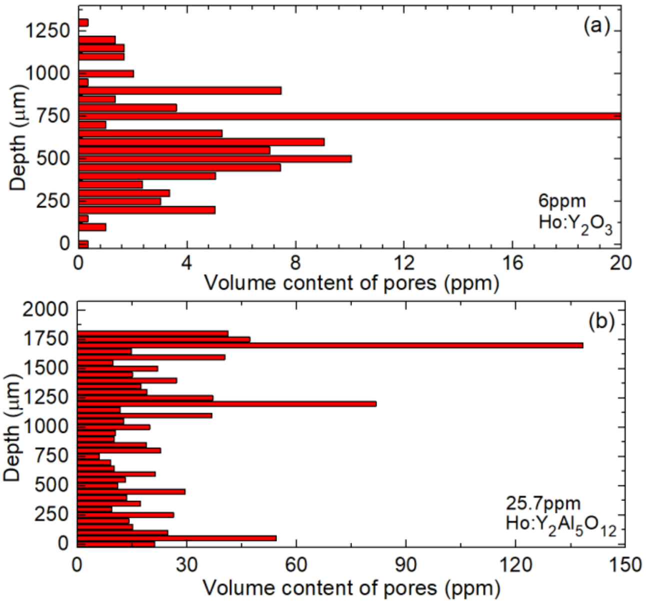

Fig. 4. Distribution of scattering centers throughout the depth of (a) Ho:Y_2O_3 and (b) Ho:$Y_3Al_5O_{12}$ ceramics.

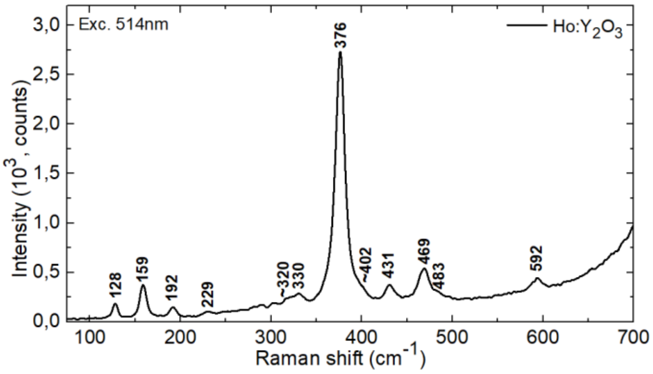

Fig. 5. RT Raman spectrum of the Ho:Y_2O_3 ceramic, *numbers* indicate the Raman frequencies in cm^{-1}, λ_{exc} = 514 nm.

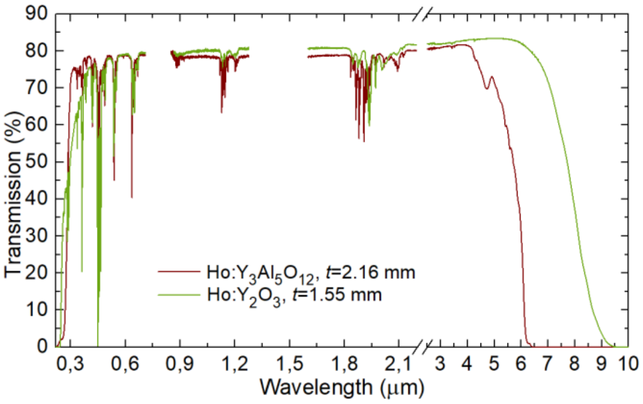

Fig. 6. In-line transmission spectra of Ho:Y_2O_3 (t = 1.55 mm) and Ho:$Y_3Al_5O_{12}$ (t = 2.16 mm) ceramic disks.

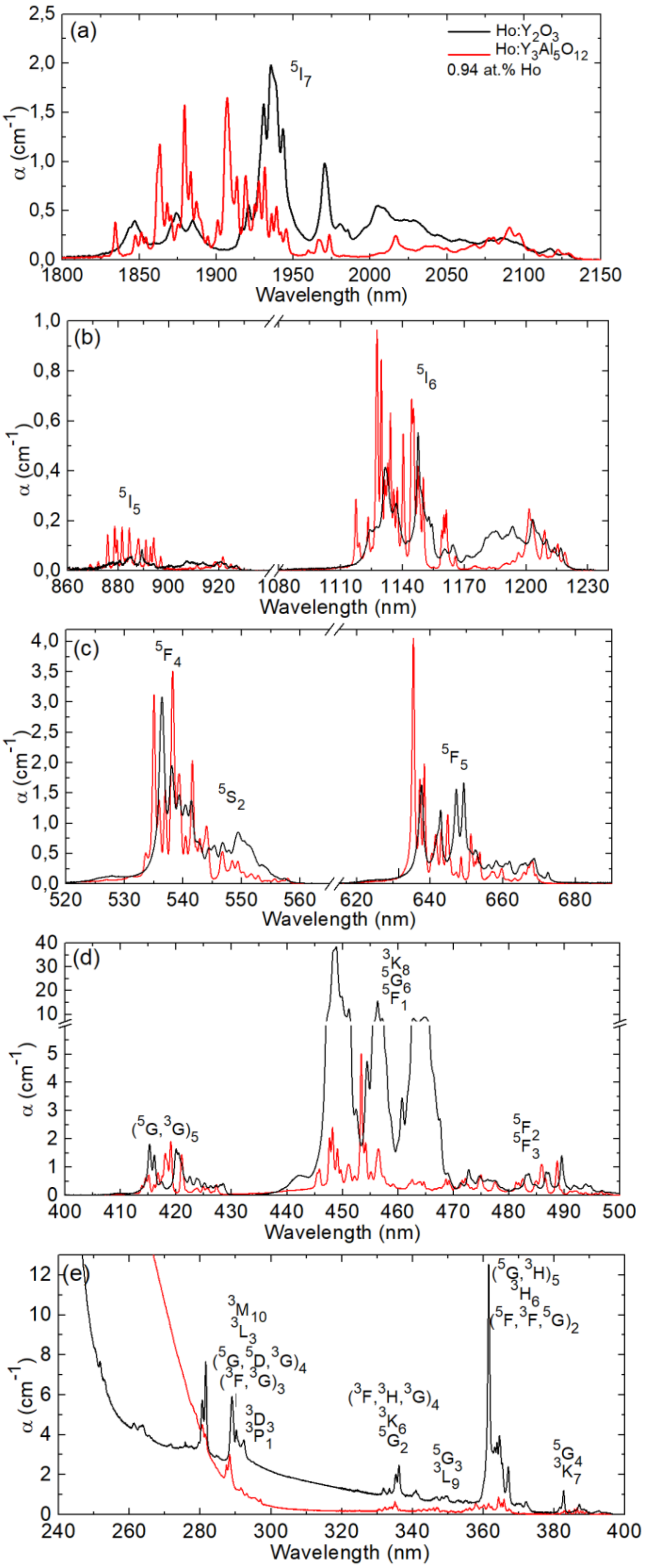

Fig. 7. (a-d) RT absorption spectra of 0.94 at.% Ho^{3+}-doped Y_2O_3 and $Y_3Al_5O_{12}$ ceramics. The band assignment is after [39].

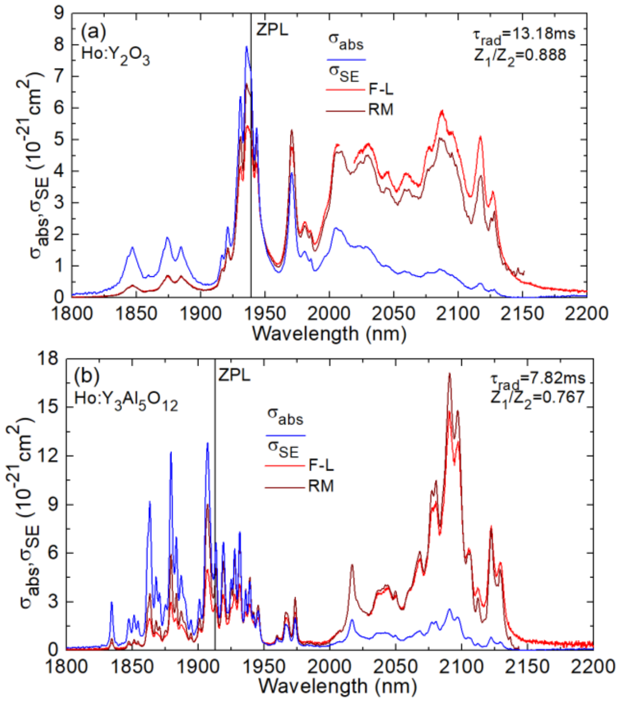

Fig. 8. RT absorption, σ_{abs}, and stimulated-emission (SE), σ_{SE}, cross-sections for the $^5I_8 \leftrightarrow {}^5I_7$ transition of Ho^{3+} ions in (a) Y_2O_3 and (b) $Y_3Al_5O_{12}$ ceramics. RM – reciprocity method, F-L - Füchtbauer–Ladenburg equation. ZPL – zero-phonon line.

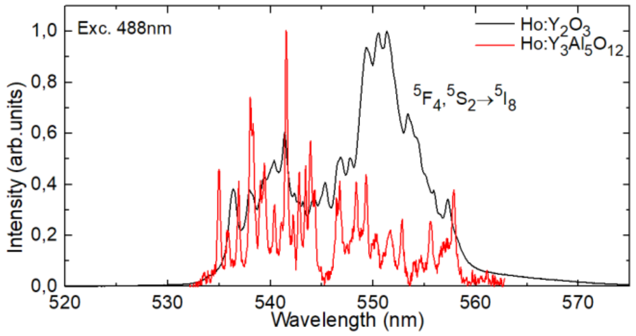

Fig. 9. Spectra of visible (green) luminescence of Ho^{3+} ions in Y_2O_3 and $Y_3Al_5O_{12}$ ceramics at RT, λ_{exc} = 488 nm.

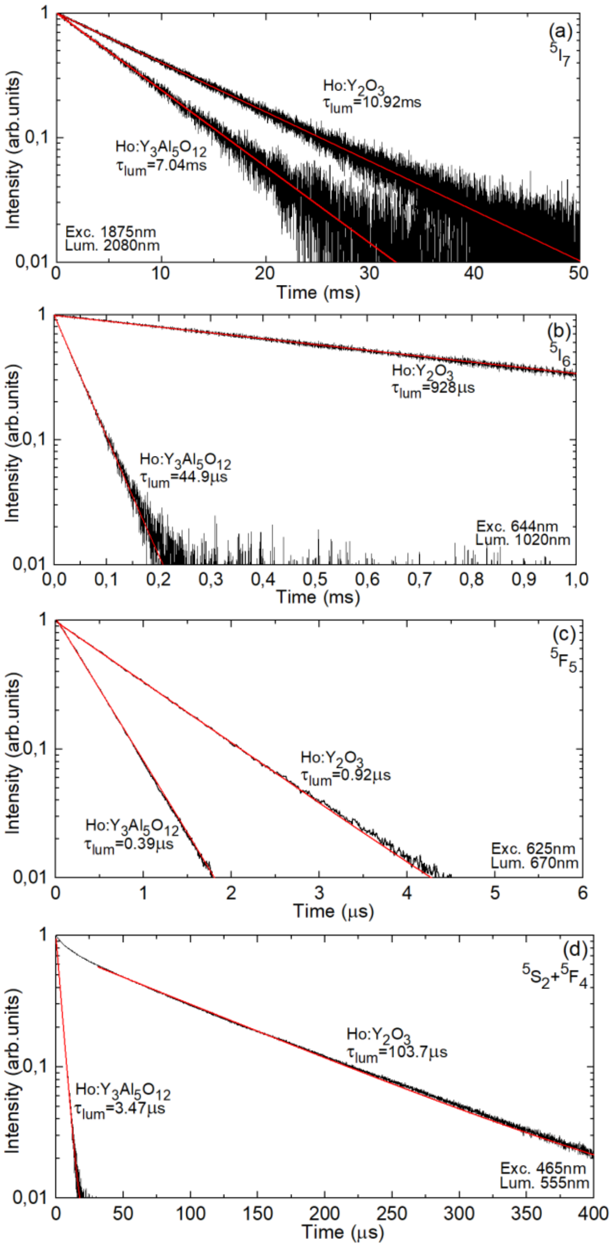

Fig. 10. RT luminescence decay curves for Ho^{3+} ions in Y_2O_3 and $Y_3Al_5O_{12}$ ceramics: decay from the (a) $^5I_7$ state, (b) $^5I_6$ state, (c) $^5F_5$ state and (d) $^5S_2$ + $^5F_4$ thermally coupled states, *black curves* – experimental data, *red lines* – single-exponential fits, τ_{lum} – luminescence decay time.

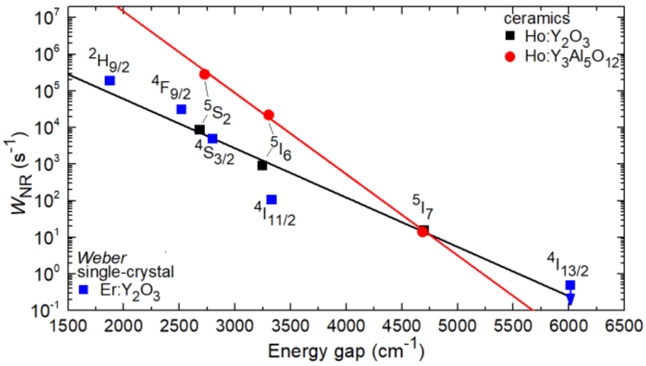

Fig. 11. Multi-phonon non-radiative relaxation rates W_{NR} as a function of the energy-gap to the lower-lying multiplet for Ho^{3+} ions in Y_2O_3 and $Y_3Al_5O_{12}$ ceramics: *symbols* – data deduced from the experimental lifetimes, *lines* – their fits using Eq. (x), *blue squares* – data from [47] for Er^{3+} ions in crystalline Y_2O_3.

Table 2. Evaluation of multi-phonon relaxation rates W_{NR} for Ho^{3+} ions in Y_2O_3 and $Y_3Al_5O_{12}$ ceramics, τ_{rad} – radiative lifetime (after [43,44]), τ_{lum} – luminescence lifetime.

Ceramic	State	τ_{rad}, ms	τ_{lum}, ms	W_{NR}, s^{-1}
Y_2O_3	$^5I_7$	13.185	10.92	15.7
	$^5I_6$	6.842	0.928	0.93×10^3
	$^5S_2$	1.378	0.104	0.89×10^4
$Y_3Al_5O_{12}$	$^5I_7$	7.82	7.04	14.2
	$^5I_6$	3.48	0.045	0.22×10^5
	$^5S_2$	0.27	0.004	0.28×10^6

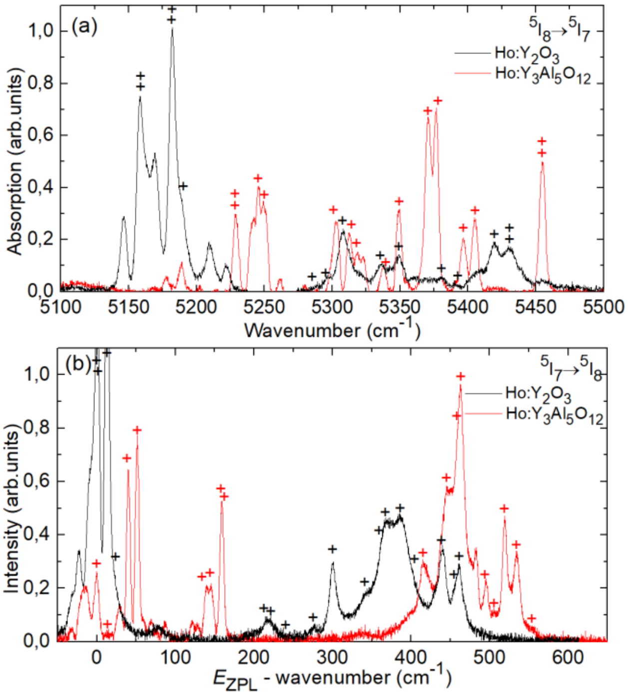

Fig. 12. LT (12 K) (a) absorption and (b) luminescence spectra for the $^5I_8 \leftrightarrow {}^5I_7$ transition of Ho^{3+} ions in Y$_2$O$_3$ and Y$_3$Al$_5$O$_{12}$ ceramics: "+" indicate peak assigned to electronic transitions of Ho^{3+} ions in C$_2$ sites (Y$_2$O$_3$) and D$_2$ sites (Y$_3$Al$_5$O$_{12}$). In (b), λ_{exc} = 532 nm.

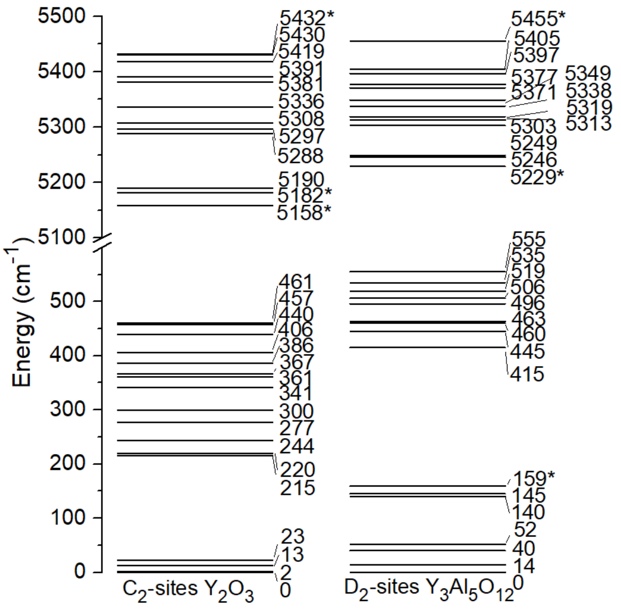

Fig. 13. Crystal-field splitting of the $^5I_8$ and $^5I_7$ Ho^{3+} multiplets in Y$_2$O$_3$ ceramics (C$_2$ sites) and Y$_3$Al$_5$O$_{12}$ ceramics (D$_2$ sites), *numbers* indicate Stark sub-level energies in cm^{-1}, *asterisks* indicate two sub-levels of the same energy.

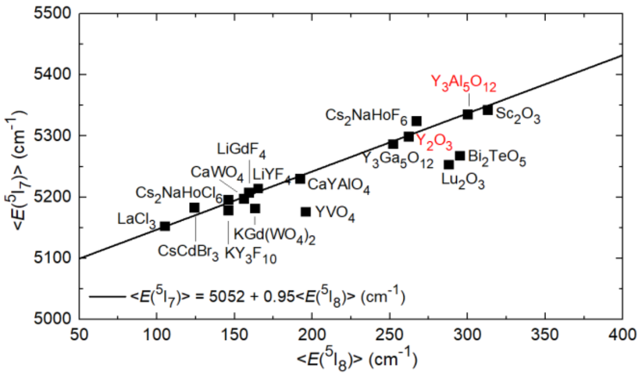

Fig. 14. Barycenter plot for $^5I_8$ and $^5I_7$ Ho^{3+} multiplets in various crystalline materials, *squares* – data on the crystal-field splitting from the literature and from this work (for Y_2O_3 and $Y_3Al_5O_{12}$ ceramics), *line* – linear fit of the data.